Electrochimica Acta 248 (2017) 425–439

Contents lists available at ScienceDirect

Electrochimica Acta

journal homepage: www.elsevier.com/locate/electacta

Pore-scale study of multiphase reactive transport in fibrous electrodes of vanadium redox flow batteries

Li Chen[a,b,*], YaLing He[a], Wen-Quan Tao[a], Piotr Zelenay[c], Rangachary Mukundan[c], Qinjun Kang[b,*]

[a] Key Laboratory of Thermo-Fluid Science and Engineering of MOE, School of Energy and Power Engineering, Xi'an Jiaotong University, Xi'an, Shaanxi, 710049, China
[b] Computational Earth Science, EES-16, Earth and Environmental Sciences Division, Los Alamos National Laboratory, Los Alamos, NM, 87544, USA
[c] Materials Synthesis and Integrated Devices, MPA-11, Materials Physics and Applications Division, Los Alamos National Laboratory, Los Alamos, NM, 87544, USA

ARTICLE INFO

Article history:
Received 29 May 2017
Received in revised form 12 July 2017
Accepted 14 July 2017
Available online 21 July 2017

Keywords:
vanadium flow battery
fibrous electrodes
permeability and diffusivity
bubble evolution
pore-scale simulation

ABSTRACT

The electrode of a vanadium redox flow battery generally is a carbon fibre-based porous medium, in which important physicochemical processes occur. In this work, pore-scale simulations are performed to study complex multiphase flow and reactive transport in the electrode by using the lattice Boltzmann method (LBM). Four hundred fibrous electrodes with different fibre diameters and porosities are reconstructed. Both the permeability and diffusivity of the reconstructed electrodes are predicted and compared with empirical relationships in the literature. Reactive surface area of the electrodes is also evaluated and it is found that existing empirical relationship overestimates the reactive surface under lower porosities. Further, a pore-scale electrochemical reaction model is developed to study the effects of fibre diameter and porosity on electrolyte flow, V_{II}/V_{III} transport, and electrochemical reaction at the electrolyte-fibre surface. Finally, evolution of bubble cluster generated by the side reaction is studied by adopting a LB multiphase flow model. Effects of porosity, fibre diameter, gas saturation and solid surface wettability on average bubble diameter and reduction of reactive surface area due to coverage of bubbles on solid surface are investigated in detail. It is found that gas coverage ratio is always lower than that adopted in the continuum model in the literature. The current pore-scale studies successfully reveal the complex multiphase flow and reactive transport processes in the electrode, and the simulation results can be further upscaled to improve the accuracy of the current continuum-scale models.

1. Introduction

The utilization of solar and wind energy has been rapidly expanded in many countries around the world. These renewable-energy sources are intermittent and often unpredictable, and integrating them into an electric grid would endanger the grid stability without required storage. Electrochemical energy storage systems are of great help for the regulation and transmission of the intermittent renewable energy. The redox flow battery (RFB) is an efficient energy storage technique with many advantages such as decoupled power and energy [1–5]. The energy storage capacity of a RFB depends on the reservoir or tank size, while its power output increases with the active electrode surface area and the number of cells. Among different types of RFBs, the vanadium redox flow battery (VRFB) perhaps has received the most attention, as it avoids the risk of contamination when ion transfers across the membrane separating the positive and negative sides [6,7]. In a VRFB, the reversible solution-phase electrochemical couples of vanadium, namely V_{II}/V_{III} and V_{IV}/V_{V}, are stored in respective tanks and circulated to the negative and positive half-cells, respectively.

The dominant losses in VRFBs, other than reaction kinetics, are related to the mass and charge transport in the electrolyte and membrane [1]. To optimize cell performance and reduce costs, great efforts have been continuously devoted to optimize the ion transports in the electrodes of VRFBs. Macroscopic continuum models are useful and efficient tools for this purpose, providing a better understanding of the complex coupled fluid flow, ion transport, electron conduction, and electrochemical reactions that

* Corresponding authors at: Computational Earth Science, EES-16, Earth and Environmental Sciences Division, Los Alamos National Laboratory, Los Alamos, NM, 87544, USA.
E-mail addresses: lichennht08@mail.xjtu.edu.cn (L. Chen), qkang@lanl.gov (Q. Kang).

http://dx.doi.org/10.1016/j.electacta.2017.07.086
0013-4686/

occur simultaneously in the VRFB electrodes [8–16]. Shah et al. proposed a 2D VRFB model which was validated by experimental results [8]. You et al. developed a 2D model for VRFB and investigated the effects of applied current density, electrode porosity and local mass transfer coefficient on the performance [9]. Non-isothermal model was also developed to study the effects of temperature [10]. Effects of oxygen and hydrogen bubbles generated by side reactions were studied in Ref. [11,12] by a multiphase mixture model. VRFB performance adopting different flow field designs were also numerically evaluated by Xu et al. [13]. In macroscopic continuum models, volumetric averaging conservation equations (mass, momentum, charge, ion and energy) are solved in each representative elementary volume assuming a homogeneous porous component with isotropic or anisotropic transport properties. The reliability and accuracy of these continuum models highly depend on a group of empirical relationships employed for determining the effective transport properties of the porous electrodes in VRFBs, such as permeability vs. porosity, effective diffusivity vs. porosity, etc. [8–16]. Accurate determination of these effective transport properties thus is critical for better prediction of the coupled physical-chemical-electrical processes in VRFBs.

One key component of VRFBs is the porous electrode where electrochemical reactions take place [17]. Fibrous materials are the favored porous-electrode substrate because they can achieve high porosity while maintaining electrical conductivity[1]. Such materials show complex microscopic porous structures, in which fibres contact, overlap or intersect with each other, leading to non-uniform pore size distributions. The aforementioned macroscopic continuum models, although allow for computationally efficient larger scale simulations, usually neglect the influence of porous structures of the electrodes and cannot capture the underlying details of transport phenomena, because the average length of a computational element in such models is much larger than typical pore size of electrodes. Alternatively, pore-scale studies provide an efficient way for in-depth understanding of the multiple processes in porous electrodes. In such pore-scale studies, the complex porous structures of the electrodes are fully resolved, and transport processes are directly accounted for. Pore-scale studies can be broadly categorized into rule-based and first-principle-based models [18,19]. For the former one, pore-network (PN) modeling approach is a typical example, in which a somewhat idealized network is adopted to represent the porous medium and simplified hydrodynamic and reactive equations are solved. On the other hand, the first-principle-based methods resolve the underlying transport processes by solving the governing equations. “Bottom-up” numerical methods, for example the lattice Boltzmann method (LBM), have the inherent capacity of accounting for the porous structures due to their remarkable ability of treating complex boundaries [20–22]. Recently, Qiu et al. [23,24] adopted the LBM to investigate pore-scale reactive transport processes in VRFB, which, to the authors’ best knowledge, are the only pore-scale numerical studies reported in the open literature regarding VRFB. In their work, porous structures of carbon-felt electrode were reconstructed from X-ray computed tomography images. A pore-scale model, which comprehensively took into account electrolyte flow, ionic species transport, charge transfer and electrochemical reactions, was developed [23,24].

The ultimate goal of our study is to develop a multi-scale simulation strategy for the reactive transport in VRFBs. For the first step in the present study, pore-scale simulations are conducted to predict some important structural and transport properties of carbon fibre-based electrodes. We also adopt the LBM, which has been developed as a powerful alternative approach for studying fluid flow and transport processes during the past two decades [20–22]. Compared with classic computational fluid dynamics methods directly based on the Navier-Stokes equation, such as finite volume method, the LBM offers two significant advantages. First, due to its kinetic nature, no-slip boundary conditions in complex geometries can be easily implemented through simple local rules such as bounce-back scheme. Second, the two main steps in the LB framework, namely collision and streaming, are purely local, leading to straightforward parallelization of the LB code. The LBM is particularly successful in applications involving interfacial dynamics such as multiphase flow and complex geometries such as porous media [25–31]. In the present study, single phase (multiphase) model, mass transport model and reactive transport model in the LB framework are adopted to investigate the multiphase flow and reactive transport processes within the electrodes. Details of each model can be found in the corresponding sections.

Hundreds of porous structures of fibrous electrodes with different porosities and fibre diameters are reconstructed (Section 2). Important properties of the electrode, including transport properties (permeability and diffusivity, Section 3) as well as volumetric reactive surface area (Section 4.1) are predicted, which can be further incorporated into macroscopic continuum-scale model to improve the model prediction capacity. Reactive transport within the electrodes with different values of porosities and fibre diameters is also studied (Section 4.2). Finally, in Section 5, pore-scale multiphase flow simulations are performed to investigate the dynamic behaviors of oxygen bubbles inside the electrodes. Effects of gas coverage of the solid surface on the reduction of reactive surface area are discussed in detail.

2. 3D porous structure reconstruction

High-resolution SEM images of VRFB electrodes provide useful information about the porous structures of the electrodes and the characteristics of the carbon fibres [32,33]. It is observed that the fibrous electrode consists of randomly distributed fibres with a cylindrical shape. Based on these SEM images, statistical information of the electrode can be obtained such as the volumetric porosity φ (ratio between void space and total volume, herein referred as porosity) and carbon fibre diameter d, which can be adopted to reconstruct the 3D porous structures of the electrode. The details of the reconstruction procedure are as follows [34]: (1) a node (i,j,k) in the 3D computational domain is randomly selected using a random number generator, (2) two azimuth angles α and β are randomly generated, (3) with the selected node and the prescribed azimuth angles, a line extending to the boundaries of the 3D domain can be determined, which is the axis of the cylinder representing a carbon fibre, (4) all the nodes in the 3D domain with the distance to the line less than the radius of a carbon fibre $d/2$ are designated as carbon fibre nodes. Now a carbon fibre with diameter d is generated in the 3D domain. Other carbon fibres are generated in the same way following Steps 1-4, until the prescribed porosity of the electrode is achieved. In the present study, electrode porosity with values from 0.5 to 0.9 with an interval of 0.1 and carbon fibre with four diameters of 6, 8, 10 and 15 μm are reconstructed. Note that the structure reconstruction algorithm relies on a random process. Therefore, the geometry as well as the properties might vary from one generated structure to another even if the input parameters are identical. To consider such variability, it is necessary to generate several geometries from the same set of input parameters. In the present study, 20 structures are generated for each configuration. Therefore, with five values of electrode porosity and four values of fibre diameter, totally 400 porous structures of electrodes are reconstructed. Fig. 1 shows four of the reconstructed structures with different porosity and fibre diameter values. The domain size is $L_x \times L_y \times L_z$, with L_x, L_y and L_z as 400, 150 and 150 μm. The resolution is 1 μm/lattice, leading to

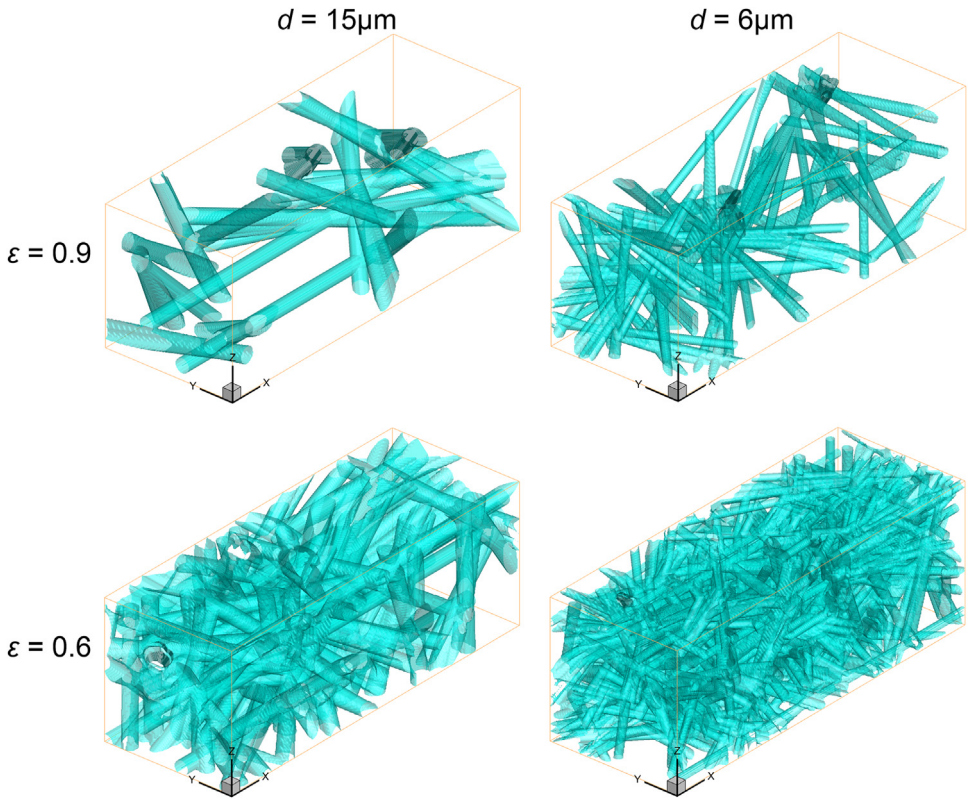

Fig. 1. Porous structures of the reconstructed fibrous electrodes with different porosity and fibre diameter.

$400 \times 150 \times 100$ lattices used in the LB simulations. As shown in Fig. 1, with a smaller diameter, more fibres are required to achieve the same porosity, leading to much more complicated porous structures of the electrodes, which will obviously affect the macroscopic transport properties of and the reaction processes in the electrodes, which will be studied in detail in the following sections.

3. Macroscopic transport properties

3.1. Permeability

Permeability is a key property describing the capacity of a porous medium for fluid to flow through. It is defined via Darcy's law in terms of the ratio of flow rate to the applied pressure

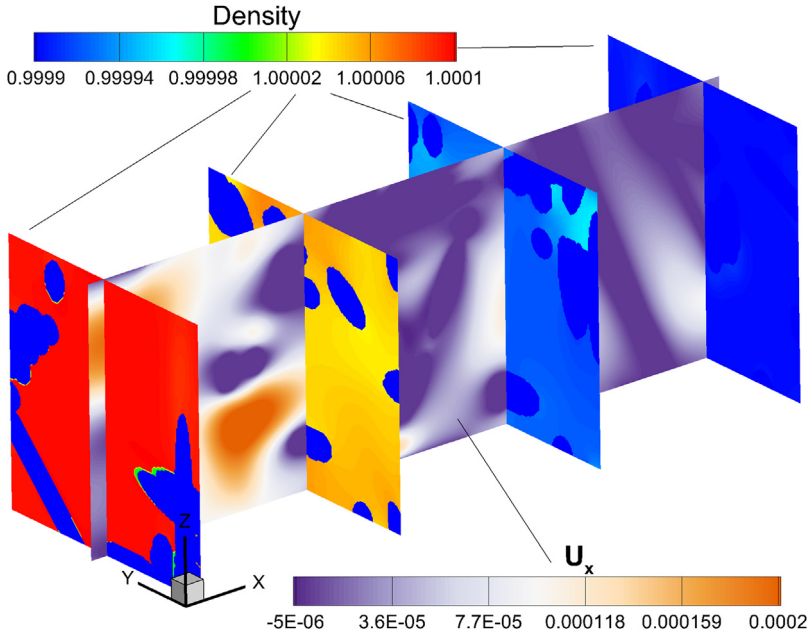

Fig. 2. Pore-scale pressure and velocity distributions in an electrode with porosity of 0.8 and fibre diameter of 15 μm.

gradient. Although permeability is a well-established property for most relatively uniform porous media, its actual dependence on complex geometries and topologies is not well understood. The values of permeability are greatly affected by the details of the porous structures, and thus it is hard to propose a generalized relationship between permeability and statistic properties of a porous medium (porosity, specific surface area, grain size, etc.). Because experimental determination of permeability is usually expensive and time-consuming, pore-scale numerical modeling, in which the complex porous structures of a porous medium is fully resolved, has been developed as a useful and efficient tool for permeability prediction. In the present study, the LBM is employed to simulate fluid flow in the electrodes of VRFBs, and the permeability is predicted based on the velocity fields obtained from the simulations. The LB fluid flow model adopted is briefly introduced as follows. For fluid flow, the evolution equation for the distribution functions can be written as

$$f_i(\mathbf{x}+\mathbf{e}_i\Delta t, t+\Delta t) - f_i(\mathbf{x},t) = \mathbf{D}[f_i^{eq}(\mathbf{x},t) - f_i(\mathbf{x},t)] \quad i = 0 \sim N, \tag{1}$$

where $f_i(\mathbf{x},t)$ is the ith density distribution function at the lattice site $\mathbf{x}$ and time t. $\mathbf{D}$ is the relaxation matrix. For the D3Q19 (three-dimensional nineteen-velocity) lattice model with $N = 18$, the discrete lattice velocity $\mathbf{e}_i$ is given by $0, i = 0$; $((\pm1, 0, 0), (0, \pm1, 0), (0, \pm1, 0))$, $i = 1 \sim 6$; and $(\pm1, \pm1, 0), (0, \pm1, \pm1), (\pm1, 0, \pm1)$, $i = 7 \sim 18$. f^{eq} is the ith equilibrium distribution function and is a function of local density and velocity

$$f_i^{eq} = w_i\rho\left[1 + \frac{\mathbf{e}_i\cdot\mathbf{u}}{(c_s)^2} + \frac{(\mathbf{e}_i\cdot\mathbf{u})^2}{2(c_s)^4} - \frac{\mathbf{u}\cdot\mathbf{u}}{2(c_s)^2}\right], \tag{2}$$

with the weight coefficient w_i as $w_i = 1/3, i = 0$; $w_i = 1/18, i = 1,2, \ldots, 6$; $w_i = 1/36$, $i = 7,8, \ldots, 18$. $c_s = 1/\sqrt{3}$ is the speed of sound. By multiplying a transformation matrix $\mathbf{Q}$ (a $(N+1)\times(N+1)$ matrix) in Eq. (1), the evolution equation in the moment space can be expressed as [35]

$$\mathbf{m}(\mathbf{x}+\mathbf{c}\Delta t, t+\Delta t) - \mathbf{m}(\mathbf{x},t) = \bar{\mathbf{S}}[\mathbf{m}^{eq}(\mathbf{x},t) - \mathbf{m}(\mathbf{x},t)], \tag{3}$$

where $\mathbf{m} = \mathbf{Q}\cdot\mathbf{f}$, $\mathbf{m}^{eq} = \mathbf{Q}\cdot\mathbf{f}^{eq}$ and $\bar{\mathbf{S}} = \mathbf{Q}\cdot\mathbf{S}\cdot\mathbf{Q}^{-1}$, with $\mathbf{m}$ and $\mathbf{m}^{eq}$ as the velocity moments and equilibrium velocity moments, respectively. $\bar{\mathbf{S}}$ is the relaxation matrix. Details of the MRT LBM can be found in Appendix A.

LB simulations are performed for the 400 reconstructed electrodes as discussed in Section 2. Boundary conditions for the LB simulation are as follows. A pressure gradient with the value of 0.0002 in LB units is applied between $x = 0$ and $x = L_x$, leading to the maximum magnitude of velocity in the electrode about 0.01 (in lattice units), meeting the low Mach number (Ma, defined as the ratio between local velocity to the speed of sound) limit of the LB fluid flow model [20]. Periodic boundary conditions are applied for the y and z directions. Fig. 2 shows the pressure and velocity distributions obtained from the LB simulations in slices of an electrode with porosity 0.8 and fibre diameter of 15 μm. The complex porous structures significantly affect the flow pattern in the pores and around the carbon fibres. It is observed that although the fluid flow mainly flows towards the positive x direction along which the pressure gradient is applied, local velocity along $-x$ direction also exists due to the effects of the local solid carbon fibres.

After the velocity field is obtained, permeability k can be calculated based on the Darcy' law

$$< u >= -\frac{k}{\mu}\nabla p \tag{4}$$

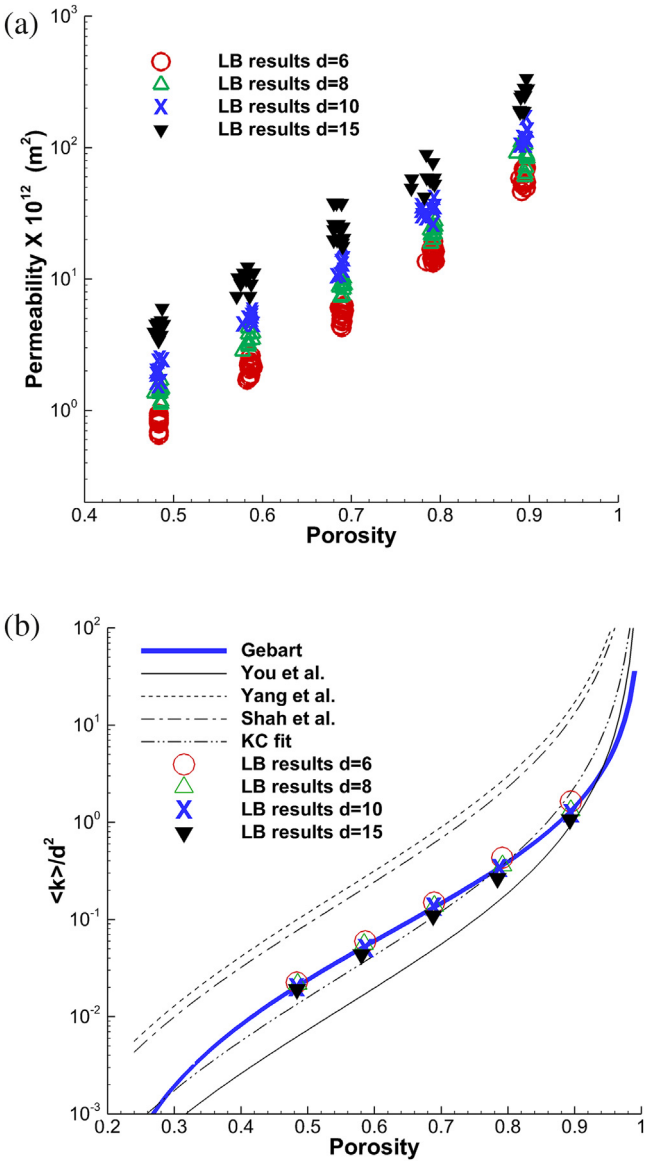

Fig. 3. Comparison between permeability predicated by the LB and that calculated using empirical relationships. (a) Permeability for all the 400 reconstructed fibrous electrodes, and (b) normalized averaged permeability.

where $<u>$ (m s^{-1}) is the volume-averaged fluid velocity along flow direction, μ (Pa s) is viscosity and ∇p (Pa m^{-1}) is pressure gradient. Fig. 3(a) shows the electrode permeability as a function of porosity and fibre diameter. Porosity is a key parameter affecting permeability. Generally as porosity increases permeability also increases, which is the case for the fibrous porous electrodes as shown in Fig. 3(a). The fibre diameter has a significant impact on the permeability. A larger fibre diameter leads to a higher permeability. For example, for $\varepsilon = 0.9$, the highest permeability for the electrode with $d = 15$ μm is about 334.6 in LB units or 3.346×10^{-10} m^2 in physical units as the length scale is 1×10^{-6} m/lattice, while that for the electrode with $d = 6$ μm is only about 71.18 in LB units or 7.118×10^{-11} m^2 in physical units. Previous studies have proposed several empirical relationships for permeability of fibrous porous media in which fibre diameter is a scaling factor [29,36–38]. For example, Gebart proposed the following empirical relationship [36]

$$\frac{k}{d^2} = \frac{C_1}{4}\left(\sqrt{\frac{1-\varepsilon_c}{1-\varepsilon}} - 1\right)^{C_2} \tag{5}$$

where ε_c is the threshold porosity under which there is no connected void space for fluid flowing. C_1 and C_2 are geometric factors, serving as fitting parameters for experimental or pore-scale simulation results. We average the permeability values of 20 reconstructed electrodes for the same set of input reconstruction parameters, namely the same ε and d, normalize the averaged value using d^2, and plot $<k>/d^2$ vs. ε in Fig. 3(b). As can be seen in Fig. 3(b), values of k/d^2 for different d almost collapse into a single curve. Using Eq. (5) the LB simulation results can be well fit with $C_1 = 1.416, C_2 = 2.202$ and $\varepsilon_c = 0.163$. Nabovati et al. [39] also performed LB simulations to predict randomly distributed fibrous media with d ranging from 4 to 12 μm. Using Eq. (5), their results lead to $C_1 = 1.974, C_2 = 2.31$ and $\varepsilon_c = 0.0743$. Recently, there have been some macroscopic numerical models proposed for studying transport phenomena in VRFBs [9–12,15]. In such macroscopic models, electrode permeability is required as an input parameter, and the Kozeny–Carmen (KC) equation is widely adopted

$$\frac{k}{d^2} = \frac{1}{aK_{CK}} \frac{\phi^3}{(1-\phi)^2} \tag{6}$$

where a is a constant and K_{CK} is the KC constant. In the study of You et al. [9], $a = 16$ and $K_{CK} = 4.28$; in the series of work by Shah an co-authors [10–12], $a = 1$ and $K_{CK} = 5.55$; and in the recent work of Yang et al. [15] $a = 1$ and $K_{CK} = 4.28$. As shown in Fig. 3(b), the discrepancy between the LB predicted permeability and that adopted in current macroscopic models is considerable. The LB simulations are based on the porous structures of the electrodes, and can be considered as benchmark results. Values of permeability in the work of Yang et al. [15] and Shah et al. [10–12] are relatively higher, and would overestimate the battery performance. A higher value of $aK_{CK} = 68.48$ was adopted in You et al. [9], and the curve of You et al. and that of Gebart intersect with each other at around 0.94, as shown in Fig. 3(b). The LB predicted permeability is also fitted using Eq. (6), and it is found that $aK_{CK} = 31.68$ leads to the best fit. However, the best fitted curve using KC equation still presents discrepancy with the LB results as shown in Fig. 3(b). This indicates KC equation, which is based on sphere particle-packed porous media, is not suitable for describing permeability-porosity relationship of fibrous porous media, which is also demonstrated in previous study [39]. The results in Fig. 3(b) suggest that Eq. (5) is recommended to calculate permeability of electrodes in VRFB in the future macroscopic continuum modeling.

3.2. Effective diffusivity

To model the ion transport in the electrolyte and calculate the effective diffusivity of fibrous electrodes, the convection-diffusion (CD) equation for concentration is solved. The LB mass transport model is adopted for this purpose. The evolution equation for the concentration distribution function is as follows [40]

$$g_i(\mathbf{x} + \mathbf{e}_i \Delta t, t + \Delta t) - g_i(\mathbf{x}, t) = -\frac{1}{\tau_g}(g_i(\mathbf{x}, t) - g_i^{eq}(\mathbf{x}, t)) \tag{7}$$

where g_i is the concentration distribution function. In the literature, for modeling species transport processes, because concentration is a scalar rather than a vector such as the velocity, a reduced lattice model, such as D3Q7 for 3D simulation, is widely adopted for species diffusion which can save the computational resources while still can maintain the accuracy [40–42]. For simple geometries or porous media with high porosity such as the fibrous electrodes considered in the present study, the D3Q7 lattice model with lattice velocity $i = 7 \sim 18$ discarded is sufficient to accurately simulate the diffusion processes and predict transport properties [43,44]. The equilibrium distribution function is as follows

$$g_i^{eq} = C(a_i + 0.5\mathbf{e}_i \cdot \mathbf{u}), \quad a_i = \begin{cases} J & i = 0 \\ (1-J)/6 & i = 1 \sim 6 \end{cases} \tag{8}$$

where J can be adjusted to obtain different diffusivities [42]. The concentration and the diffusivity are obtained by $C = \sum g_i$ and $D = (1-J)(\tau_g - 0.5)\Delta x^2/3\Delta t$, respectively. When using the above LB mass transport model to predict effective diffusivity, pure diffusion process is considered and thus velocity in Eq. (8) is zero. In Section 4.2 where coupled fluid flow, ion transport, and electrochemical reactions on fibre-electrolyte interface are all considered, velocity will be included. The boundary conditions for pure ion diffusion simulations are no flux at the electrolyte-fibre interface, prescribed concentration at inlet $x = 0$ and outlet $x = L_x$ of the computational domain, and periodic boundary conditions for the other four boundaries (y and z directions). The effective diffusivity D_{eff} along the x direction is calculated from the steady-state concentration fields obtained from the LB simulations.

$$D_{eff} = \frac{(\int_0^{L_y}\int_0^{L_z}(D_{bulk}\frac{\partial C}{\partial x})|_{L_x} dydz)/L_yL_z}{(C_{in} - C_{out})/L_x} \tag{9}$$

where C_{in} and C_{out} are the inlet and outlet concentration, respectively. $|_{L_x}$ means local value at $x = L_x$. Fig. 4 shows the numerically computed effective diffusivity of the 400 reconstructed fibrous electrodes as a function of porosity. Note that D_{eff} is normalized by D_{bulk}. While the fibre diameter significantly affects the permeability as discussed in Section 3.1, its influence on the effective diffusivity is insignificant as shown in Fig. 4. This is reasonable considering the different mechanisms of flow and diffusion. In the macroscopic continuum-scale models of VRFB [9,11–13,15], Bruggeman's correlation is widely adopted for determining D_{eff}

$$D_{eff} = \varepsilon^{\alpha} D_{bulk} \tag{10}$$

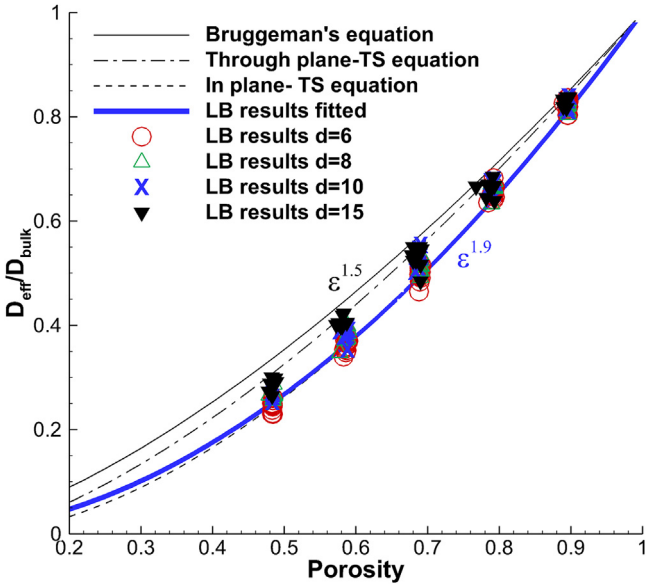

Fig. 4. Comparison between the effective diffusivity predicated by the LB and that calculated by empirical relationships.

with $\alpha = 1.5$. Besides, for fibrous media with layered-fibre structures, Todamakis and Sotirchos (TS) proposed the following empirical relationship [45]

$$D_{\text{eff}} = D_{\text{bulk}}\varepsilon\left[\frac{\varepsilon - 0.11}{1 - 0.11}\right]^{\beta} \quad (11)$$

Because the structures of layered-fibre materials are anisotropic, the value of β for through-plane and in-plane directions is different, which is 0.785 and 0.521, respectively [45]. Both Eqs. (10) and (11) are plotted in Fig. 4. It can be seen that generally the Bruggeman's equation and through-plane TS equation produce higher D_{eff} compared with the simulated results. The in-plane TS equation is in good agreement with the simulated results. Fitting the LB predicted D_{eff} using Eq. (10), α is determined as 1.9, higher than 1.5 adopted in the original Bruggeman's equation, indicating more complex structures and more tortuous void space in the fibrous electrodes. It is worth mentioning that in proton exchange membrane fuel cell where layered-fibre materials are widely used for gas diffusion layer (GDL), it is also commonly found that D_{eff} of GDL is lower than that predicted by the original Bruggeman's equation with $\alpha = 1.5$ [46].

4. Reactive transport

4.1. Reactive surface area

Electrochemical reactions take place at the solid-electrolyte interface as schematically shown in the top image of Fig. 5(a), and V_{II} is converted into V_{III} in the negative half-cell during discharging, with generated electrons transferring from the negative electrode through the external circuit to the positive electrode

$$V_{II} \rightarrow V_{III} + e^{-} \quad (12)$$

Obviously, for the surface reaction described in Eq. (12), the area of the electrolyte-fibre interface plays an important role [1]. Higher interface area is required to promote the electrochemical reaction. The top image of Fig. 5(a) schematically shows the electrolyte-fibre interface. In our study, square lattices are adopted to discretize the computational domain, therefore a curve boundary will be approximately represented by stair-step lines. At the pore-scale, different interface nodes have different number of reactive surfaces. As shown in Fig. 5(a), interface nodes A, B and C have three, two and one reactive surfaces, respectively (see the read lines). Volumetric reactive surface area $\bar{s}$, defined as the ratio of the total effective interface area to the total fibre volume S/V_f, is determined based on the reconstructed electrode structures and is plotted in the bottom image of Fig. 5(a). Here, effective interface area is the area of the interface which directly contacts with open void space percolating the porous electrodes. This means that "dead end" pores in the domain are excluded because reactants cannot be supplied to these pores (See top image of Fig. 5(a)). The algorithms in Ref. [40] is adopted to distinguish the percolating void space and the "dead end" pores. As shown in Fig. 5(a), $\bar{s}$ decreases as the fibre volume fraction increases (or the porosity decreases), because more and more fibres overlap, contact or intersect with each other (See Fig. 1). Besides, $\bar{s}$ increases as the fibre diameter reduces under the same fibre volume fraction, because $\bar{s}$ is proportional to d^{-1}. Note that surface roughness which can increase $\bar{s}$ is not considered in this study.

In the macroscopic continuum models, reactive surface area is an input parameter required for modeling the electrochemical reactions [9,12,15]. In the volumetric averaging conservation equation of mass (details can be found in Ref. [9]) in each computational cell, reactive surface area per cell volume is calculated. Therefore, to match the volumetric surface area

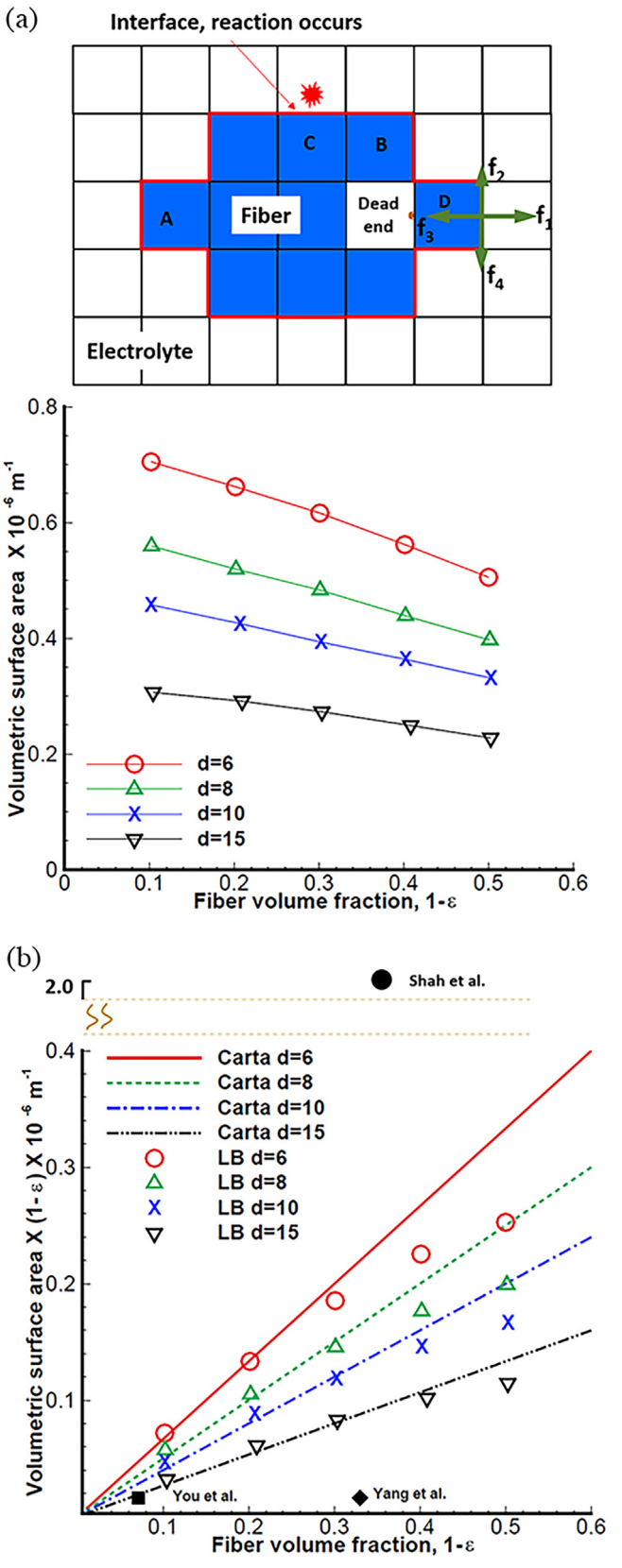

Fig. 5. Volumetric surface area of the fibrous electrodes in VRFBs. (a) Top image: schematic of the electrolyte-fibre interface and Bottom image: relationship between volumetric surface area and fibre volume fraction for electrodes with different fibre diameters. (b) comparisons between pore-scale results, the empirical relationship and the values chosen in the literature.

employed in the macroscopic models with the present pore-scale results, $\bar{S}$ discussed in Fig. 5(a) should be modified as $\hat{s}$, and the relationship between the two is

$$\hat{s} = \frac{S}{V_{cell}} = \frac{S}{V_f}\frac{V_f}{V_{cell}} = \bar{s}(1-\varepsilon) \tag{13}$$

Based on the assumption of a filament analogue model, Garta et al. proposed the following formula to compute $\hat{s}$ [47]

$$\hat{s} = \frac{4}{d}(1-\varepsilon) \tag{14}$$

Fig. 5(b) displays $\hat{s}$ based on our reconstructed fibrous electrodes and that calculated value using the simple model of Eq. (14). The change trends of the two are similar: $\hat{s}$ increases as ε decreases under the same d, and $\hat{s}$ increases as d decreases under the same ε. Compared with Fig. 5(a), the change trend of $\hat{s}$vs. (1-ε) and that of $\bar{s}$ vs. (1-ε) is different, as expected. Under a low fibre volume fraction, the values of $\hat{s}$ for the present study and that calculated using Eq. (14) are in good agreement; however, the discrepancy increases as the fibre volume fraction gets higher. This is because for a lower fibre volume fraction, there are fewer fibres in the domain which have lower chance to overlap, contact or intersect, and thus the reconstructed electrode structures can be approximately described by the filament analogue model of Carta et al. [47]. However, as the fibre volume fraction increases, there are increasing numbers of fibres in the domain, which tend to contact, overlap or intersect, thereby reducing the surface area. Under such a scenario, the filament analogue model fails. Thus, the values of $\hat{s}$ in the present study is lower than that predicted by Eq. (14) under higher fibre volume fraction. The discrepancy decreases as the fibre diameter increases, consistent with the above discussions because for higher fibre diameter, fewer fibres are needed to achieve the same fibre volume fraction, thus the probability of contact, overlap or intersect will be lower. Therefore, if one uses Eq. (14) to determine the volumetric reactive surface area, a correction factor should be added under higher fibre volume fraction (or lower porosity).

Different values of $\hat{s}$ are chosen in the continuum models in the literature. In the work of You et al. [9], $\hat{s} = 1.6\times10^4\,m^{-1}$ with $\varepsilon = 0.929$, in Yang et al.'s work [15] $\hat{s} = 1.6\times10^4\,m^{-1}$ with $\varepsilon = 0.67$ and in Shah et al.'s work [12], $\hat{s} = 2\times10^6\,m^{-1}$ with $\varepsilon = 0.67$. These values are also plotted in Fig. 5(b). As shown in Fig. 5(b), the value in Ref. [9] is close to the present study and that predicted using Eq. (14), while that in Ref. [15] is a little lower and that in Ref. [12] is significantly higher. For surface electrochemical reactions taking place in VRFBs, it is desirable to have a higher reactive surface area. Hence, lower fibre diameter is preferred based on Fig. 5. However, lower fibre diameter results in lower permeability and higher flow resistance (see Fig. 3(a)), slowing down the convective transport of the reactant to the electrolyte-fibre interface. Therefore, there is a balance between increasing reactive surface area and reducing pressure drop and pumping cost.

4.2. Reactive transport modeling

Coupled single-phase electrolyte flow, multiple ion transport and electrochemical reactions in the negative electrodes of VRFB during discharging process are investigated in this section. Several factors, including porous structures of the electrode, the reactive surface area, the local V_{II} and V_{III} concentrations, and the transport rate of V_{II} and V_{III}, play roles in the reactive transport processes. Emphasis is placed on the effects of pore-scale structures of the fibrous electrodes. Convection-diffusion equation is solved for V_{II} and V_{III} transport. Strictly speaking, the Nernst–Planck equation, a mass conversation equation for describing the motion of charged chemical species including an additional flux caused by the electric filed, should be solved. In the literature, this additional flux term is commonly neglected as its effect is insignificant [9].

During discharging process in VRFB, sulfuric acid solutions containing vanadium ions in the storage tank are pumped into the battery. Correspondingly, for fluid flow simulation at the pore-scale, a pressure drop is applied at the inlet and outlet of the reconstructed electrodes to drive the electrolyte flow. Concentration boundary conditions are adopted for all species at the inlet ($x = 0$). A parameter named SOC, which is defined as the charge state of the cell, is introduced to determine inlet concentrations of V_{II} and V_{III} [10]

$$C_{II} = SOC\cdot C_0, \quad C_{III} = (1-SOC)\cdot C_0 \tag{15}$$

where C_0 is the initial vanadium concentration of the negative half-cell. The initial vanadium solution in the negative half-cell is 2000 mol m^{-3} $V_2(SO_4)_3$, thus $C_0 = 2000\,mol\,m^{-3}$. At the outlet, fully developed boundary conditions are adopted, namely the gradient of concentration is zero

$$\frac{\partial C_{II}}{\partial x}|_{x=L_x} = 0, \ \frac{\partial C_{III}}{\partial x}|_{x=L_x} = 0 \tag{16}$$

The rate of reaction Eq. (12) at the electrolyte-fibre interface is as follows based on the Bulter–Volmer model

$$D\frac{\partial C_{II}}{\partial n} = -k(C_{II})^{0.5}(C_{III})^{0.5}\left[\exp(\frac{0.5F\eta}{RT}) - \exp(-\frac{0.5F\eta}{RT})\right] \tag{17a}$$

$$D\frac{\partial C_{III}}{\partial n} = k(C_{II})^{0.5}(C_{III})^{0.5}\left[\exp(\frac{0.5F\eta}{RT}) - \exp(-\frac{0.5F\eta}{RT})\right] \tag{17b}$$

where R, T and F are gas constant, temperature and Faraday's constant, respectively. η is the overpotential, defined as the difference between the electrode potential under current flow and the zero current potential. Due to high electron conductivity in the fibre and the relatively small computational domain, η is assumed to be uniform at the electrolyte-fibre interface, an additional assumption made in the present pore-scale studies. It is worth pointing out that in the macroscopic continuum-scale models, an additional term C_S/C_{Bulk}, defined as the ratio of surface concentration to bulk concentration, is added before the two natural exponent functions in Eq. (17). These additional terms are employed to describe the mass transfer between the bulk solution and the electrolyte-fibre interface which cannot be solved in a computational cell in the continuum-scale models [9]. They, however, are not required in our pore-scale studies, as the mass transfer between the bulk solution and the electrolyte-fibre interface is directly solved.

Several LB boundary conditions have been proposed for surface reaction in the literature [42,48,49], and the one proposed by Kang et al. is adopted [48] in which the non-equilibrium part of the distribution functions is demonstrated to have equal value but opposite sign. For an electrolyte-fibre interface node such as D in Fig. 5(a), the following set of equations can be obtained for its reactive surface [48]

$$\begin{cases} f_{C_{II},1} - f_{C_{II},3} = -k^{0.5}0.5\left[\exp(\frac{0.5F\eta}{RT}) - \exp(-\frac{0.5F\eta}{RT})\right] \text{(a)} \\ f_{C_{II},1} + f_{C_{II},3} = \frac{(1-J)}{3}C_{II} \text{(b)} \\ f_{C_{III},1} - f_{C_{III},3} = k^{0.5}0.5\left[\exp(\frac{0.5F\eta}{RT}) - \exp(-\frac{0.5F\eta}{RT})\right] \text{(c)} \\ f_{C_{III},1} + f_{C_{III},3} = \frac{(1-J)}{3}C_{III} \text{(d)} \end{cases} \tag{18}$$

where the unknown variables are $f_{C_{II},1}$, $f_{C_{III},1}$, C_{II} and C_{III}. Combing Eq. (8), after some simple algebraic operations, the following

Table 1
Parameter values used in the simulation [6,9].

Physicochemical variables		Value of Physical unit	Value of lattice unit
Kinematics viscosity	υ	$4.928\times10^{-6}\,m^2\,s^{-1}$	1/6
Diffusivity of C_{II} and C_{III}	D	$2.4\times10^{-10}\,m^2\,s^{-1}$	1/7
SOC		0.8	0.8
Inlet concentration C	C_0	$2000\,mol\,m^{-3}$	2
Reaction rate constant	k	$1.7\times10^{-7}\,m\,s^{-1}$	1.01×10^{-4}
Porosity	ε	0.9	0.9
Fiber diameter	d	15 μm	15
Overpotential	η	0.08V	0.08

equation for C_{II} can be obtained

$$\left[\frac{(1-J)^3}{27}+\frac{1}{3}k^2(1-J)\right]{C_{II}}^2 - \left[\frac{4(1-J)^2}{9}f_{C_{II},3}+2k^2(f_{C_{II},3}+f_{C_{III},3})\right]C_{II}+\frac{4}{3}(1-J){f_{C_{II},3}}^2 = 0 \quad (19)$$

Newton–Raphson method is used to iteratively solve Eq. (19) with initial value of C_{II} as the value of previous time step. After C_{II} is determined, the other three unknown variables can be readily solved.

The general procedures for the pore-scale simulations are as follows. (1) Fluid flow LB model introduced in Section 3.1 is adopted to solve the electrolyte flow. (2) Using the flow filed obtained, ion transport is solved using the LB mass transport model introduced in Section 3.1 with LB reactive boundary condition given by Eq. (18). The simulation is considered to be converged when the relative error of interested variables such as concentration is lower than a prescribed tolerance which is 1×10^{-8} in this study. Values of the variables for the base case are listed in Table 1. Fig. 6 shows the concentration field of V_{II} and V_{III} in electrodes with different fibre diameter, where the electrode porosity is 0.9. According to results in previous sections, as fibre diameter decreases, the reactive surface area increases and the permeability decreases, both of which lead to more V_{II} consumed and more V_{III} generated. It is found that $C_{II}(d=6\,\mu m)$ is only 0.234 of $C_{II}(d=15\,\mu m)$ while $C_{III}(d=6\,\mu m)$ is 2.22 times higher than $C_{III}(d=15\,\mu m)$. Effects of the porosity are also explored, and the results are displayed in Fig. 7, where the fibre diameter is kept at 15 μm. It can be seen that porosity has a significant effect on the reactive transport. Lower porosity indicates a lower permeability and higher reactive surface area, resulting in a more rapid depletion of V_{II}, in agreement with the continuum simulation results in the literature [9].

5. Multiphase flow

During charging, side reactions generate hydrogen and oxygen bubbles inside negative and positive electrodes, respectively. Presence of bubbles inside electrodes will disturb the electrolyte flow, reduce the iron effective diffusivity, and decrease the reactive surface, thus playing complicated roles on both charging and discharging processes. It was found that oxygen evolution can cause a drop of charge efficiency by 5–10% [11]. In this section, pore-scale two phase flow simulations are performed using the LBM to simulate dynamic behaviors of oxygen bubbles within the microscopic structures of the positive electrode. Effects of porosity, fibre diameter, wettability and saturation on gas migration are explored in detail. The numerical method adopted is the pseudopotential two-phase LB model developed by Shan and Chen [50], which is widely used due to its simplicity and versatility [22]. Its basic idea is to represent the microscopic molecular interactions at the mesoscopic scale using a *pseudo-potential* (also often called effective mass) depending on the local density. With such interactions, fluid with multiple components spontaneously segregates into different phases. Such automatic phase separation is an attractive characteristic of the pseudopotential model, as the

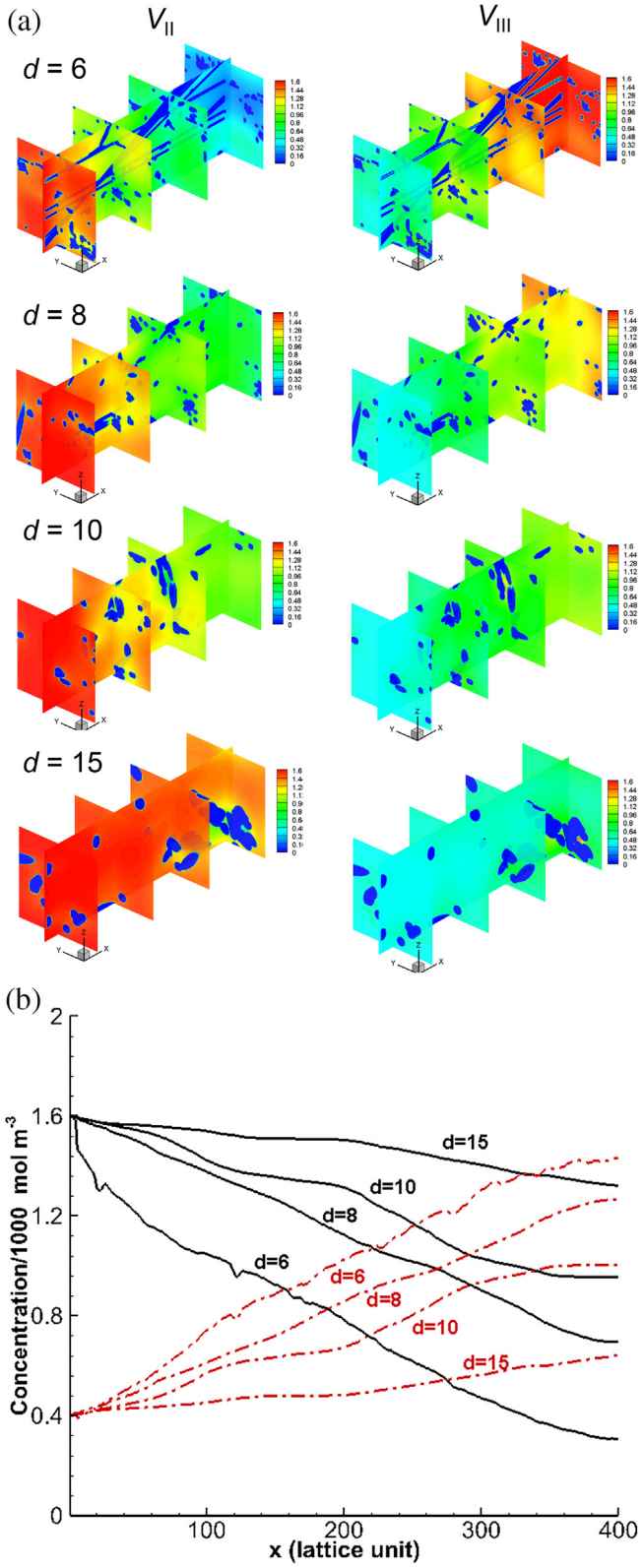

Fig. 6. Concentration distributions of C_{II} and C_{III} in electrodes with the same porosity but different fibre diameter. (a) Concentration distributions of C_{II} and C_{III} in electrodes and (b) averaged concentration along *x* direction.

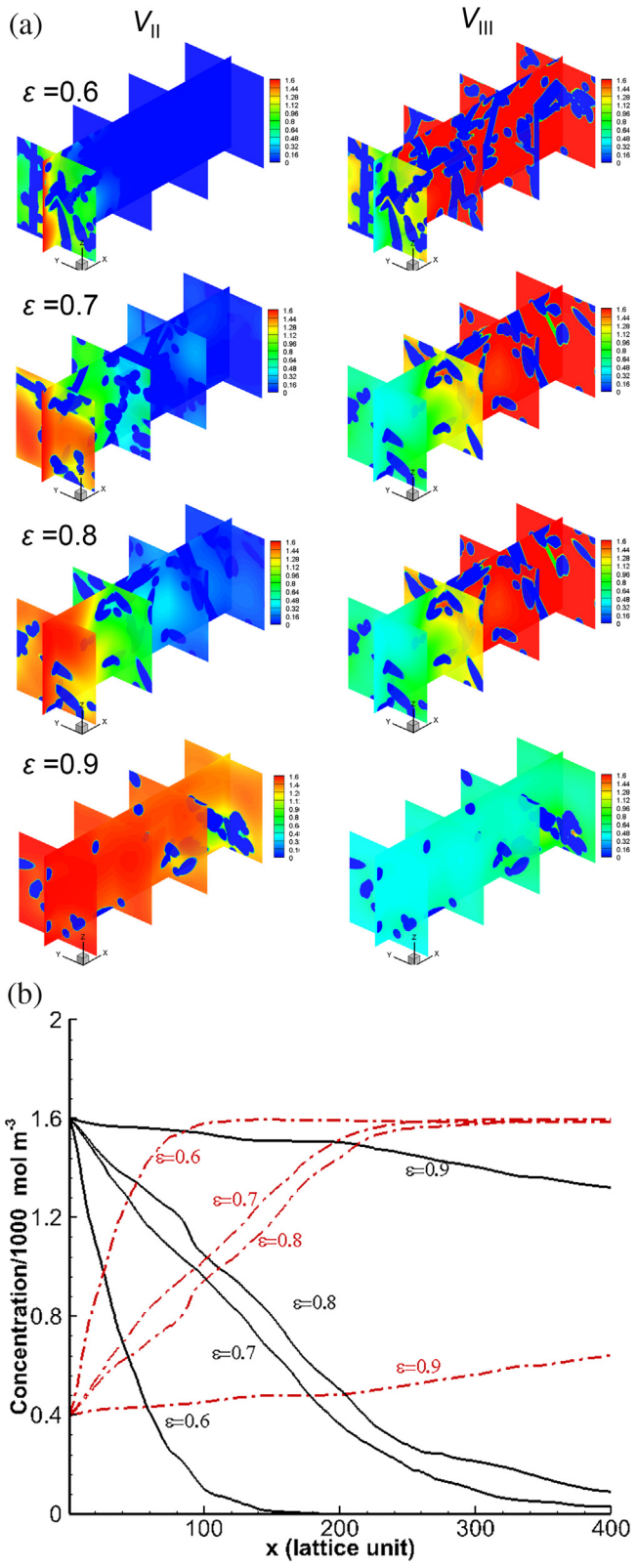

Fig. 7. Concentration distributions of C_{II} and C_{III} in electrodes with the same fibre diameter but different porosity. (a) Concentration distributions of C_{II} and C_{III} in electrodes and (b) averaged concentration along x direction.

phase interface is no longer a mathematical boundary and no explicit interface-tracking or interface-capturing technique is needed. The phase interface is a post-processed quantity that can be detected through monitoring the variation of the fluid densities [22]. The pseudopotential model has been successfully applied to a broad range of sciences such as energy, environment, chemistry, biology and geology [22]. Details of the MRT pseudopotential multiphase model with the explicit forcing scheme can be found in Appendix B.

In the simulations, fully periodic boundary conditions are applied for all the three directions. Initially, the gas and electrolyte phase are randomly distributed in the pores. This is achieved by generating a random number $\xi \in (0,1)$ at each pore node, and if ξ is less than the prescribed gas saturation α_g, the node is assigned as a gas node, otherwise it is an electrolyte node. In such way, the desired gas saturation is obtained. An external force along z direction is adopted to drive the two-phase flow. For the definition of external force, one can refer to Appendix B. Note that when the external driving force is small, two-phase flow is dominated by capillary force. The capillary number, Ca, is a dimensionless number representing the relative strength of viscous force to surface tension force $Ca = u\mu/\sigma$. For low Ca, typically less than 10^{-6}, capillary force dominates and there is no viscous coupling between different phases. Only after the external driving force is greater than a critical value, the viscous force becomes dominant [51]. Two-phase flow in VRB electrodes is relatively fast for flow-through electrode design [11,12]. Therefore in the present study, an external force of $F_e = 10^{-4}$ in lattice units along z direction is applied. The corresponding Ca is calculated as 5.56×10^{-4}, following the definition as $Ca = F_e/\sigma$, namely the ratio of external body force to the interfacial force [52].

Fig. 8 shows the oxygen evolutions in a 100*100*200 μm fibrous electrode with porosity of 0.8 and fibre diameter of 6 μm. The oxygen saturation α_g is 10%, a reasonable value between 2% and 13% as predicted by the continuum model [11]. In practice, electrode that is hydrophilic to electrolyte is desirable and thus the contact angle for oxygen is set as 147° at the solid fibre surface. At $t = 5000$ in Fig. 8, plenty of separated oxygen bubbles are randomly distributed within the pores of electrodes. Using the 19 direction connected phase labeling algorithm [43], it is estimated that the number of bubbles is 24 and the averaged bubble diameter is 17.4 μm. As the bubbles move along positive z direction, bubble-bubble interaction as well as bubble-solid interaction lead to complicated bubble evolutions, such as coalescence, separation, squeeze, trapping, elongation, etc. (from $t = 30000$ to $t = 90000$). The formation and break of the slender necks, shown in red circles from $t = 30000$ to $t = 40000$, indicates strong viscous coupling between gas and electrolyte, which was accounted in the continuum multiphase mixture model using a slip velocity [12]. Gas coverage ratio $\delta_g = A_{g\text{-}s}/A_s$, defined as the ratio between gas-solid interface area $A_{g\text{-}s}$ to the entire solid surface area A_s, is used to measure the coverage of the electrode surface by oxygen bubbles. δ_g determined from the pore-scale results is about 0.108 at $t = 5000$. Such low value is reasonable considering the hydrophobic solid surface to the oxygen bubbles. Fig. 9 further shows the temporal evolutions of the gas coverage ratio δ_g, in which δ_g has been normalized by gas saturation. After an initial stage, periodic fluctuation of the curves is shown, in agreement with the periodic boundary conditions adopted. It can be seen that the highest value of δ_g/α_g for $\alpha_g = 10\%$ is only about 0.32, with averaged value of about 0.219. Further, higher saturation cases of $\alpha_g = 20\%$ and $\alpha_g = 30\%$ are also studied, as shown in Fig. 9. With α_g increases, the gas has a higher chance to contact with the solid surface, leading to slightly higher averaged δ_g/α_g of about 0.276 and 0.29 for $\alpha_g = 20\%$ and 30%, respectively.

Effects of fibre diameter are studied. Fig. 10 shows the bubble distributions in a fibrous electrode with fibre diameter of 10 μm and other parameters the same as that in Fig. 8. There are 10 bubbles at $t = 5000$ with averaged bubble diameter about 22.8 μm. Compared with that in Fig. 8, such lower bubble number and

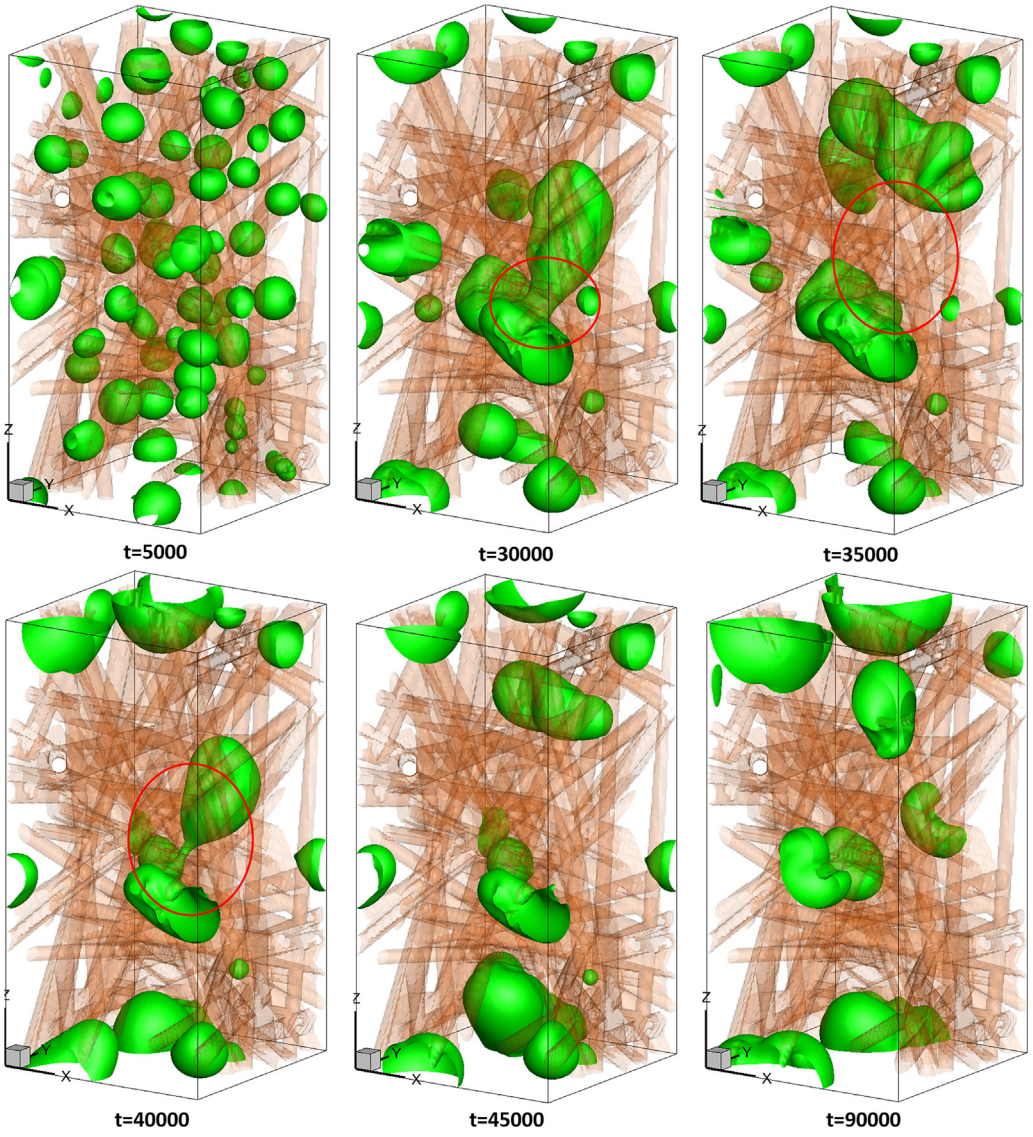

Fig. 8. Oxygen bubble evolution in a fibrous electrode with porosity of 0.8 and fibre diameter of 6 μm.

higher bubble diameter is expected, due to more connected void space and larger pore diameter generated by thicker fibres under the same porosity. Fig. 11 shows temporal evolutions of δ_g/α_g for four fibre diameter of 6 μm, 8 μm, 10 μm and 15 μm. As fibre diameter decreases, the pore size decreases, thus gas has a higher chance to contact with the solid fibre, leading to higher gas coverage ratio. Further, effects of electrode porosity are also investigated. Fig. 12 shows the simulation results in a fibrous electrode with porosity of 0.7. The other parameters are the same as that in Fig. 8. A lower porosity results in narrow void space, making it harder for bubbles to move and merge, leading to higher bubble number of 38 and lower averaged bubble diameter of about 16.65 μm compared with that in Fig. 8. A lower porosity also leads to a higher gas coverage ratio, as shown in Fig. 13. Finally, effect of contact angle is investigated and the results are shown in Fig. 14. As the contact angle increases, the gas coverage ratio decreases, as expected.

Fig. 15 displays the averaged gas coverage ratio for different fibre diameter, saturation and porosity, in which all the trends agree with above discussion. In the continuum multiphase mixture model developed by Shah [12], δ_g/α_g is set as unity. However, based on the present pore-scale prediction, δ_g/α_g is much lower than unity. Even for the case with α_g as high as 0.3, which is impractical as the maximum α_g predicted in Ref. [12] is about 0.15, δ_g/α_g is about 0.42. For these cases with $\alpha_g = 0.1$, the highest δ_g/α_g is about 0.30 (the case with diameter of 6 μm and porosity of 0.7). Obviously, if the solid fibre is less hydrophobic to oxygen, it is expected that δ_g/α_g will increase (see Fig. 14). Considering the extremely scenario with contact angle of 90°, $\delta_g/\alpha_g(\theta = 90^\circ)$ can be roughly calculated by $(\sin(180^\circ - \theta))^{-2}\delta_g/\alpha_g(\theta_{\text{ref}} = 147^\circ)$. Correspondingly, the highest δ_g/α_g will be about 1.0 for the case with diameter of 6 μm and porosity of 0.7, which is the value chosen in Ref. [12]. Therefore, among all the effects of gas bubbles generated by side reactions, if only the reduction of reactive surface by gas coverage is considered, we believe that the adverse effect of gas evolution on battery performance is overestimated in current continuum-scale numerical studies. A lower δ_g/α_g in the form of $minmum[(\sin(180^\circ - \theta))^{-2}\delta_g/\alpha_g(\theta_{\text{ref}} = 147^\circ), 1]$ is thus recommend to be adopted in the continuum model.

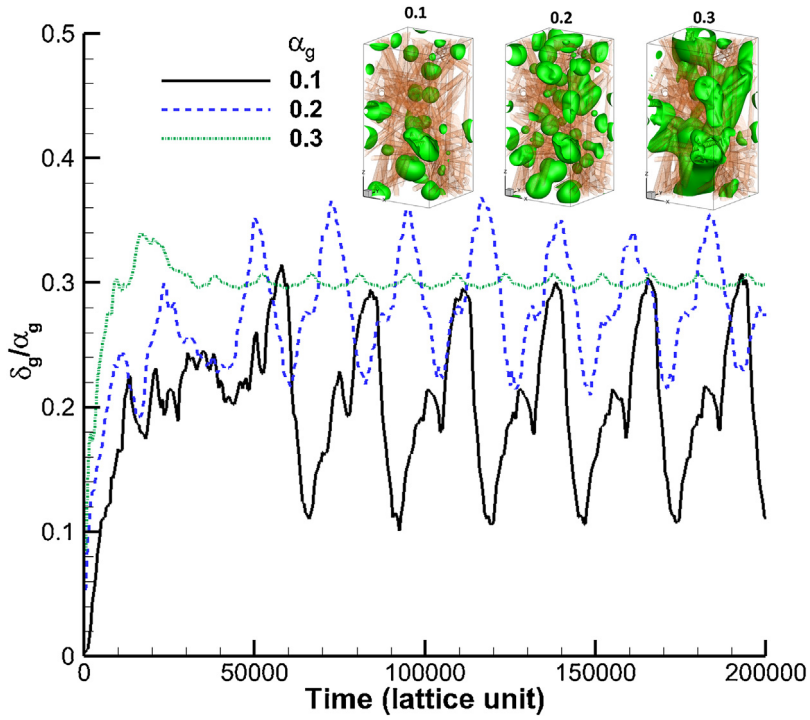

Fig. 9. Temporal evolutions of the gas coverage ratio δ_g/α_g for different gas saturation.

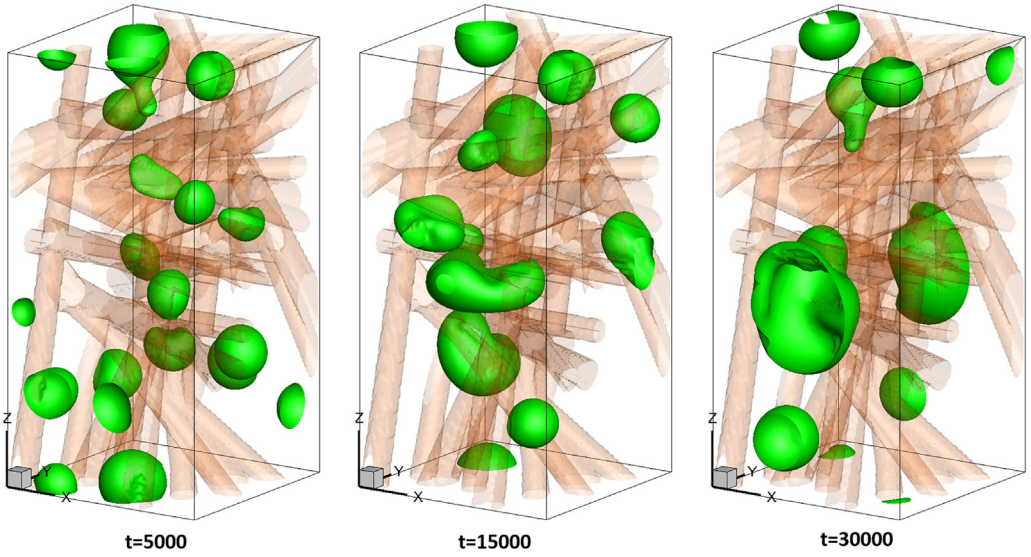

Fig. 10. Oxygen bubble evolution in a fibrous electrode with porosity of 0.8 and fibre diameter of 10 μm.

6. Conclusion

In this work, multiphase flow and reactive transport in the fibrous electrodes of VRFB is simulated using the LBM. Four hundred simulated electrode samples are reconstructed using the stochastic method by considering different electrode porosities and fibre diameters. Intrinsic permeability of the electrodes is predicted and compared with existing empirical relationships. It is found that the empirical relationship proposed by Gebart [36] is in better agreement with our pore-scale simulation results and hence is recommended to be adopted. Effective diffusivity of the electrodes is also predicted and simulation results show that Bruggeman equation with a higher exponent of 1.9 is suggested. Volumetric surface area of the electrodes is also evaluated based on the reconstructed porous electrodes, and it is found that the filament analogue model overestimates the volumetric surface area under high fibre volume fraction.

A reactive transport model for electrodes is developed, which considers electrolyte flow, V_{II} and V_{III} transport and electrochemical reaction at the electrolyte-fibre interface. The boundary condition for surface electrochemical reaction is derived in the LB framework. It is found that as fibre diameter decreases, the reactive surface area increases and the permeability decreases, causing V_{II} to be consumed more efficiently V_{III} to be generated

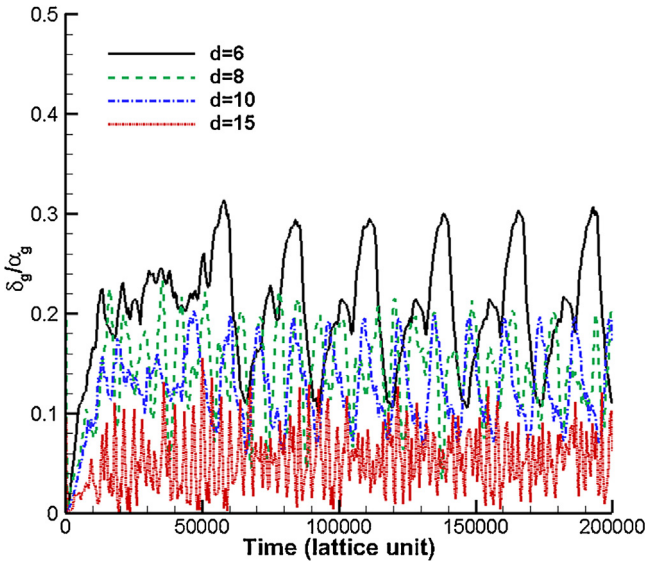

Fig. 11. Temporal evolutions of δ_g/α_g for different fibre diameter.

more efficiently. Besides, a lower porosity indicates a lower permeability and higher reactive surface area, resulting in a more rapid depletion of V_{II}.

Finally, pore-scale multiphase flow simulations were conducted to investigate oxygen bubble evolution under different porosities, fibre diameters, gas saturations and solid surface wettabilities. Complicated bubble-bubble and bubble-solid wall interactions generate complex dynamic behavior of oxygen bubbles. Effects of gas coverage on the reduction of reactive surface area are investigated in detail. It is found that gas coverage ratio is lower than that adopted in the continuum model in the literature. Reasonable values of gas coverage ratio are recommended based on the pore-scale simulation results.

Future work about VRFB electrode includes fully understand effects of important factors, such as compression, surface wettability and electrochemical properties and electrolyte properties, on the reactive transport in the electrode. Upscaling the pore-scale results to improve the prediction capability of continuum-scale models is also highly required.

Acknowledgements

The authors thank the support of National Nature Science Foundation of China (51406145), National key research and development program (2017YFB0102702), Innovative Talents Support Plan of China Postdoctoral Foundation and the Fundamental Research Funds for the Central Universities. The authors also acknowledge the support of LANL's LDRD Program and Institutional Computing Program.

Appendix A.

The equilibrium velocity moments $\mathbf{m}^{eq}$ are as follows [35]

$$\mathbf{m}_0^{eq} = \rho \tag{A1a}$$

$$\mathbf{m}_1^{eq} = -11\rho + 19\frac{\mathbf{j}\cdot\mathbf{j}}{\rho_0}, \quad \mathbf{m}_2^{eq} = 3\rho - \frac{11\mathbf{j}\cdot\mathbf{j}}{2\ \rho_0} \tag{A1b}$$

$$\mathbf{m}_3^{eq} = j_x, \quad \mathbf{m}_4^{eq} = -\frac{2}{3}j_x \tag{A1c}$$

$$\mathbf{m}_5^{eq} = j_y, \quad \mathbf{m}_6^{eq} = -\frac{2}{3}j_y \tag{A1d}$$

$$\mathbf{m}_7^{eq} = j_z, \quad \mathbf{m}_8^{eq} = -\frac{2}{3}j_z \tag{A1e}$$

$$\mathbf{m}_9^{eq} = \frac{3j_x^2 - \mathbf{j}\cdot\mathbf{j}}{\rho_0}, \quad \mathbf{m}_{10}^{eq} = -\frac{3j_x^2 - \mathbf{j}\cdot\mathbf{j}}{2\rho_0} \tag{A1f}$$

$$\mathbf{m}_{11}^{eq} = \frac{j_y^2 - j_z^2}{\rho_0}, \quad \mathbf{m}_{12}^{eq} = -\frac{j_y^2 - j_z^2}{2\rho_0} \tag{A1g}$$

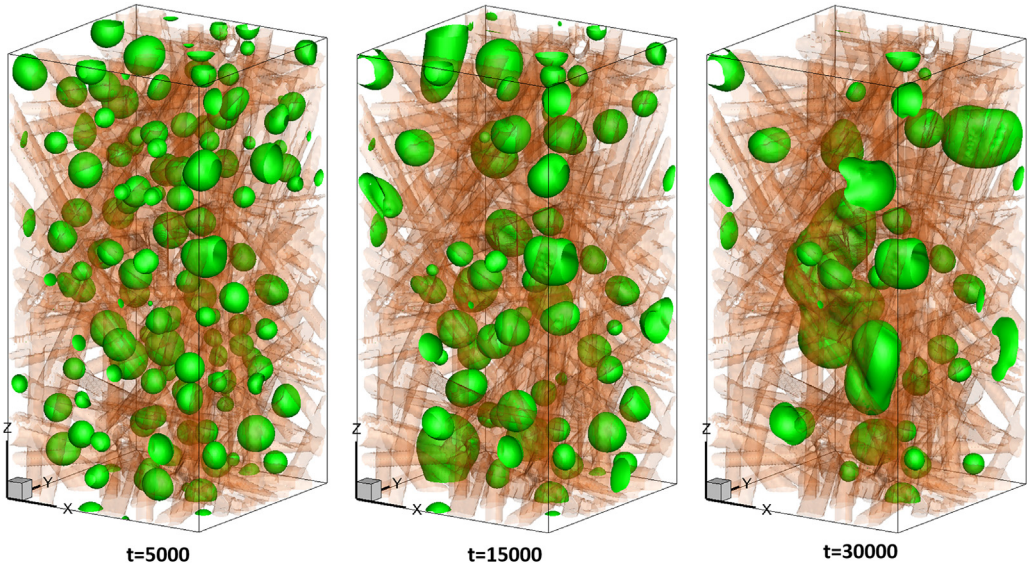

Fig. 12. Oxygen bubble evolution in a fibrous electrode with porosity of 0.7 and fibre diameter of 6 μm.

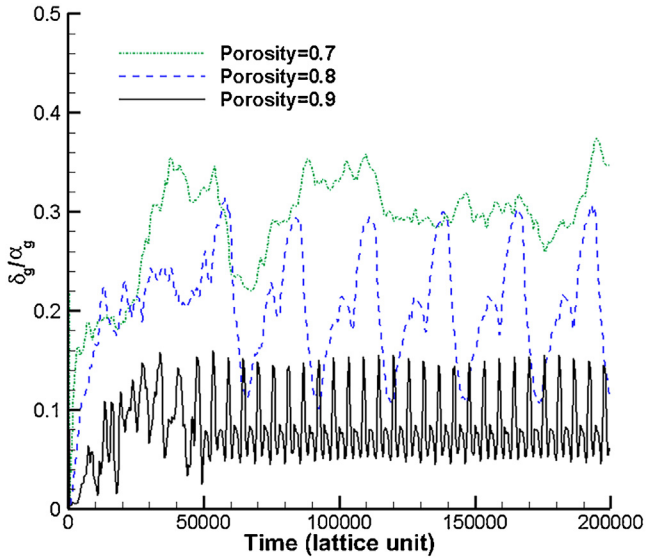

Fig. 13. Temporal evolutions of δ_g/α_g for different electrode porosity.

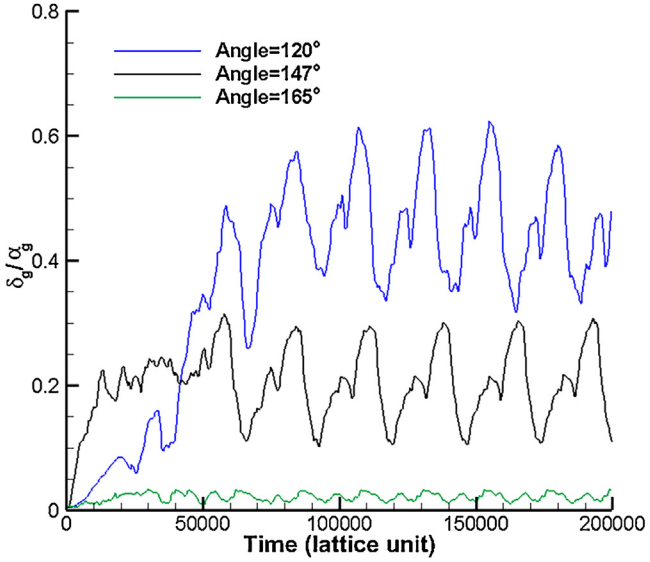

Fig. 14. Temporal evolutions of δ_g/α_g for different contact angle.

$$\mathbf{m}_{13}^{eq}=\frac{j_x j_y}{\rho_0},\quad \mathbf{m}_{14}^{eq}=\frac{j_y j_z}{\rho_0},\quad \mathbf{m}_{15}^{eq}=\frac{j_x j_z}{\rho_0} \tag{A1h}$$

$\mathbf{Q}^{-1}$ is the inverse matrix of $\mathbf{Q}$. The transformation matrix $\mathbf{Q}$ is constructed based on the principle that the relaxation matrix $\overline{\mathbf{S}}$(a $(N+1)\times(N+1)$ matrix) in moment space can be reduced to the diagonal matrix [35], namely

$$\overline{\mathbf{S}}=\mathrm{diag}(s_0,s_1,\ldots,s_{17},s_{18}), \tag{A2a}$$

$$s_0=s_3=s_5=s_7=0, s_1=s_2=s_{9-15}=\frac{1}{\tau},\ s_4=s_6=s_8=s_{16-18}=8\frac{2\tau-1}{8\tau-1}, \tag{A2b}$$

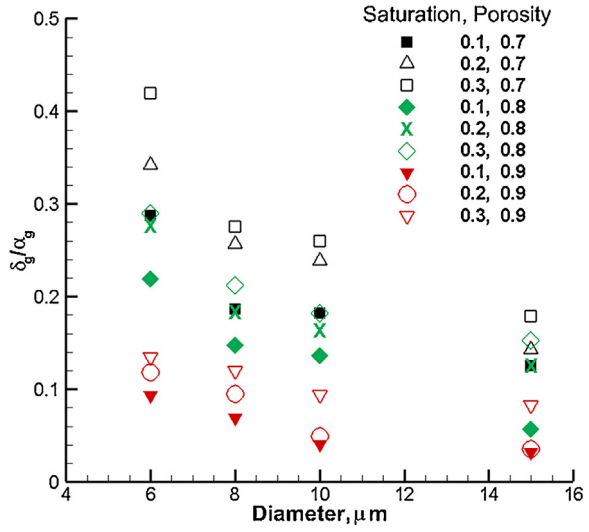

Fig. 15. The averaged δ_g/α_g for different fibre diameter, saturation and porosity.

The relaxation time τ is related to the fluid viscosity, and density and momentum are determined by sum of distribution functions

$$\tau=\frac{\upsilon}{c_s^2\Delta t}+0.5,\quad \rho=\sum_i f_i,\quad \mathbf{j}=\sum_i f_i\mathbf{e}_i \tag{A3}$$

Appendix B.

The explicit forcing (EF) scheme has been demonstrated to overcome some limitations of the original velocity shifting scheme in SC model such as high spurious currents and low viscosity ratio. The evolution of the density distribution function for kth component with MRT and EF adopted are as follows [53]

$$f_i^k(\mathbf{x}+c\mathbf{e}_i\Delta t,t+\Delta t)-f_i^k(\mathbf{x},t) = -(\mathbf{Q}^{-1}\cdot\overline{\mathbf{D}}k\cdot\mathbf{Q})[f_i^k(\mathbf{x},t)-f_i^{eq,k}(\mathbf{x},t)]+\delta t\left(\mathbf{Q}^{-1}\cdot(\mathbf{I}-\frac{\overline{\mathbf{D}}k}{2})\cdot\mathbf{Q}\right)f_i^{F,k}(\mathbf{x},t) \tag{B1}$$

The equilibrium distribution functions f^{eq} for kth component are as follows

$$f_i^{eq,k}=\omega_i\rho_k\left[1+\frac{3}{c^2}(\mathbf{e}_i\cdot\mathbf{u}_k^{eq})+\frac{9}{2c^4}(\mathbf{e}_i\cdot\mathbf{u}_k^{eq})^2-\frac{3}{2c^2}(\mathbf{u}_k^{eq})^2\right] \tag{B2}$$

The diagonal relaxation matrix is defined as

$$\overline{\mathbf{D}}^k=\mathrm{diag}\left[s_c^k,s_e^k,s_\varepsilon^k,s_c^k,s_q^k,s_c^k,s_q^k,s_\upsilon^k,s_\upsilon^k\right] \tag{B3}$$

s_c^k corresponds to the conserved moments and is set as one in our simulations. s_e^k, s_ε^k and s_q^k correspond to non-conserved moments, and they are free parameters which can be adjusted to improve the accuracy and stability of the MRT model. In our simulations, the values of these free parameters are as follows: $s_e^k=0.6$, $s_\varepsilon^k=1.5$ and $s_q^k=1.2$. s_υ^k is related to the viscosity of the kth component fluid

$$\upsilon^k=\frac{1}{3}\left(\frac{1}{s_\upsilon^k}-0.5\right)\frac{\Delta x^2}{\Delta t} \tag{B4}$$

With the EF force scheme, the forcing term in Eq. (B1) is defined as

$$f_i^{F,k}=\frac{\mathbf{F}^k\cdot(\mathbf{e}_i-\mathbf{u}^{eq})}{\rho^k c_s{}^2}f_i^{eq,k} \tag{B5}$$

$\mathbf{u}^{eq}$, the effective velocity, in Eq. (B5) is calculated by

$$\mathbf{u}^{eq} = \sum s_c^k \rho^k \mathbf{u}^k / \sum s_c^k \rho^k \tag{B6}$$

which also equals $\mathbf{u}_k^{eq}$in Eq. (B2). Density and velocity of each component are determined by

$$\rho^k = \sum f_i^k, \rho^k \mathbf{u}^k = \sum f_i^k \mathbf{e}_i + \frac{\delta t}{2}\mathbf{F}^k \tag{B7}$$

and the total density and physical velocity of the fluid mixture are calculated by

$$\rho = \sum \rho^k, \mathbf{u} = \sum \rho^k \mathbf{u}^k / \sum \rho^k \tag{B8}$$

$\mathbf{F}^k$ in Eq. (B5) is the total force acting on kth component including fluid-fluid interaction force, fluid-solid interaction force and possible external body force such as gravity

$$\mathbf{F}^k = \mathbf{F}_f^k + \mathbf{F}_s^k + \mathbf{F}_e^k \tag{B9}$$

The total fluid–fluid surface tension force acting on the particles of the kth component at lattice site $\boldsymbol{x}$ is defined as

$$\mathbf{F}_f^k = -\psi^k\left(\rho^k(\mathbf{x})\right) g_f \sum_{\mathbf{x}'} \sum_{\bar{k}}^{s} w(\mathbf{x}') \psi^k\left(\rho^{\bar{k}}(\mathbf{x}')\right)(\mathbf{x}' - \mathbf{x}) \tag{B10}$$

ψ is the effective mass or the pseudopotential, which is defined as as $\psi_k(\rho_k) = 1\text{-}\exp(\text{-}\rho_k)$ in our simulations. g_f controls the strength between fluids, and mixing between different components can be adjusting by changing g_f. $w(\mathbf{x}')$ are the weights. If only the interactions of four nearest neighbors with $|\mathbf{x}' - \mathbf{x}|^2 = 1$ and the four next-nearest neighbors $|\mathbf{x}' - \mathbf{x}|^2 = 2$ are considered, $w(1) = 1/3$ and $w(2) = 1/12$. The fluid-solid interaction force is introduced to describe the interaction between kth fluid and solid walls

$$\mathbf{F}_s^k = -\psi^k\left(\rho^k(\mathbf{x})\right) g_s \sum_{\mathbf{x}'} w(\mathbf{x}') s(\mathbf{x}')(\mathbf{x}' - \mathbf{x}) \tag{B11}$$

where s is an indicator function and equals 0 and 1 for pore and solid, respectively. The coefficient g_s, which controls the strength between fluid and wall, is positive for non-wetting fluid and negative for wetting fluid. Different wettability (contact angle) can be obtained by adjusting G_s. With the EF force scheme Eq. (B5) and the MRT collision operator adopted, the original pseudopotential multicomponent multiphase phase LB model has been greatly improved in the following three aspects: reduced spurious velocities of one to two magnitudes, increased viscosity ratio up to 1000 and viscosity-independent equilibrium densities in a wide range. These improvements greatly promote the applications of pseudopotential multicomponent multiphase phase LB model, especially for multiphase flow problems with high kinematic viscosity ratio.

References

[1] A. Weber, M. Mench, J. Meyers, P. Ross, J. Gostick, Q. Liu, Redox flow batteries: a review, J Appl Electrochem 41 (2011) 1137–1164.
[2] M. Skyllas-Kazacos, M.H. Chakrabarti, S.A. Hajimolana, F.S. Mjalli, M. Saleem, Progress in Flow Battery Research and Development, Journal of The Electrochemical Society 158 (2011) R55–R79.
[3] W. Wang, Q. Luo, B. Li, X. Wei, L. Li, Z. Yang, Recent Progress in Redox Flow Battery Research and Development, Advanced Functional Materials 23 (2013) 970–986.
[4] P. Leung, X. Li, C.P.d. León, L. Berlouis, C.T.J. Low, F.C. Walsh, Progress in redox flow batteries, remaining challenges and their applications in energy storage, RSC Advances 27 (2012) 10125–10156.
[5] L.F. Arenas, C. Ponce de León, F.C. Walsh, Engineering aspects of the design, construction and performance of modular redox flow batteries for energy storage, Journal of Energy Storage 11 (2017) 119–153.
[6] E. Sum, M. Rychcik, M. Skyllas-kazacos, Investigation of the V(V)/V(IV) system for use in the positive half-cell of a redox battery, Journal of Power Sources 16 (1985) 85–95.
[7] M. Rychcik, M. Skyllas-Kazacos, Characteristics of a new all-vanadium redox flow battery, Journal of Power Sources 22 (1988) 59–67.
[8] A.A. Shah, M.J. Watt-Smith, F.C. Walsh, A dynamic performance model for redox-flow batteries involving soluble species, Electrochimica Acta 53 (2008) 8087–8100.
[9] D. You, H. Zhang, J. Chen, A simple model for the vanadium redox battery, Electrochimica Acta 54 (2009) 6827–6836.
[10] H. Al-Fetlawi, A.A. Shah, F.C. Walsh, Non-isothermal modelling of the all-vanadium redox flow battery, Electrochimica Acta 55 (2009) 78–89.
[11] H. Al-Fetlawi, A.A. Shah, F.C. Walsh, Modelling the effects of oxygen evolution in the all-vanadium redox flow battery, Electrochimica Acta 55 (2010) 3192–3205.
[12] A.A. Shah, H. Al-Fetlawi, F.C. Walsh, Dynamic modelling of hydrogen evolution effects in the all-vanadium redox flow battery, Electrochimica Acta 55 (2010) 1125–1139.
[13] Q. Xu, T.S. Zhao, P.K. Leung, Numerical investigations of flow field designs for vanadium redox flow batteries, Applied Energy 105 (2013) 47–56.
[14] A.A. Shah, R. Tangirala, R. Singh, R.G.A. Wills, F.C. Walsh, A Dynamic Unit Cell Model for the All-Vanadium Flow Battery, Journal of The Electrochemical Society 158 (2011) A671–A677.
[15] W.W. Yang, Y.L. He, Y.S. Li, Performance Modeling of a Vanadium Redox Flow Battery during Discharging, Electrochimica Acta 155 (2015) 279–287.
[16] M.J. Watt-Smith, P. Ridley, R.G.A. Wills, A.A. Shah, F.C. Walsh, The importance of key operational variables and electrolyte monitoring to the performance of an all vanadium redox flow battery, Journal of Chemical Technology & Biotechnology 88 (2013) 126–138.
[17] F.C. Walsh, L.F. Arenas, C. Ponce de León, G.W. Reade, I. Whyte, B.G. Mellor, The continued development of reticulated vitreous carbon as a versatile electrode material: Structure, properties and applications, Electrochimica Acta 215 (2016) 566–591.
[18] L. Chen, Y.-L. Feng, C.-X. Song, L. Chen, Y.-L. He, W.-Q. Tao, Multi-scale modeling of proton exchange membrane fuel cell by coupling finite volume method and lattice Boltzmann method, International Journal of Heat and Mass Transfer 63 (2013) 268–283.
[19] P.P. Mukherjee, Q. Kang, C.-Y. Wang, Pore-scale modeling of two-phase transport in polymer electrolyte fuel cells-progress and perspective, Energy & Environmental Science 4 (2011) 346–369.
[20] S.Y. Chen, G.D. Doolen, Lattice Boltzmann methode for fluid flows, Ann Rev Fluid Mech 30 (1998) 329–364.
[21] C.K. Aidun, J.R. Clausen, Lattice-Boltzmann method for complex flows, Ann Rev Fluid Mech 42 (2010) 439–472.
[22] L. Chen, Q. Kang, Y. Mu, Y.-L. He, W.-Q. Tao, A critical review of the pseudopotential multiphase lattice Boltzmann model: Methods and applications, Int J Heat Mass Tran 76 (2014) 210–236.
[23] G. Qiu, C.R. Dennison, K.W. Knehr, E.C. Kumbur, Y. Sun, Pore-scale analysis of effects of electrode morphology and electrolyte flow conditions on performance of vanadium redox flow batteries, Journal of Power Sources 219 (2012) 223–234.
[24] G. Qiu, A.S. Joshi, C.R. Dennison, K.W. Knehr, E.C. Kumbur, Y. Sun, 3-D pore-scale resolved model for coupled species/charge/fluid transport in a vanadium redox flow battery, Electrochimica Acta 64 (2012) 46–64.
[25] J. Zhang, Lattice Boltzmann method for microfluidics: models and applications, Microfluidics and Nanofluidics 10 (2011) 1–28.
[26] D. Sun, M. Zhu, J. Wang, B. Sun, Lattice Boltzmann modeling of bubble formation and dendritic growth in solidification of binary alloys, International Journal of Heat and Mass Transfer 94 (2016) 474–487.
[27] Q. Kang, P.C. Lichtner, D. Zhang, Lattice Boltzmann pore-scale model for multicomponent reactive transport in porous media, Journal of Geophysical Research: Solid Earth 111 (2006).
[28] N.S. Martys, H. Chen, Simulation of multicomponent fluids in complex three-dimensional geometries by the lattice Boltzmann method, Physical Review E 53 (1996) 743–750.
[29] A. Koponen, D. Kandhai, E. Hellén, M. Alava, A. Hoekstra, M. Kataja, K. Niskanen, P. Sloot, J. Timonen, Permeability of Three-Dimensional Random Fiber Webs, Physical Review Letters 80 (1998) 716–719.
[30] L. Chen, W. Fang, Q. Kang, J. De'Haven Hyman, H.S. Viswanathan, W.-Q. Tao, Generalized lattice Boltzmann model for flow through tight porous media with Klinkenberg's effect, Physical Review E 91 (2015) 033004.
[31] L. Hao, P. Cheng, Lattice Boltzmann simulations of anisotropic permeabilities in carbon paper gas diffusion layers, Journal of Power Sources 186 (2009) 104–114.
[32] H. Zhou, H. Zhang, P. Zhao, B. Yi, A comparative study of carbon felt and activated carbon based electrodes for sodium polysulfide/bromine redox flow battery, Electrochimica Acta 51 (2006) 6304–6312.
[33] W.H. Wang, X.D. Wang, Investigation of Ir-modified carbon felt as the positive electrode of an all-vanadium redox flow battery, Electrochimica Acta 52 (2007) 6755–6762.
[34] L. Chen, H.-B. Luan, Y.-L. He, W.-Q. Tao, Pore-scale flow and mass transport in gas diffusion layer of proton exchange membrane fuel cell with interdigitated flow fields, International Journal of Thermal Sciences 51 (2012) 132–144.
[35] D. d'Humières, Multiple-relaxation-time lattice Boltzmann models in three dimensions, Philosophical Transactions of the Royal Society of London A: Mathematical, Physical and Engineering Sciences 360 (2002) 437–451.
[36] B.R. Gebart, Permeability of Unidirectional Reinforcements for RTM, Journal of Composite Materials 26 (1992) 1100–1133.

[37] D.S. Clague, B.D. Kandhai, R. Zhang, P.M.A. Sloot, Hydraulic permeability of (un) bounded fibrous media using the lattice Boltzmann method, Physical Review E 61 (2000) 616–625.
[38] M.M. Tomadakis, T.J. Robertson, Viscous Permeability of Random Fiber Structures: Comparison of Electrical and Diffusional Estimates with Experimental and Analytical Results, Journal of Composite Materials 39 (2005) 163–188.
[39] A. Nabovati, E.W. Llewellin, A.C.M. Sousa, A general model for the permeability of fibrous porous media based on fluid flow simulations using the lattice Boltzmann method, Composites Part A: Applied Science and Manufacturing 40 (2009) 860–869.
[40] L. Chen, G. Wu, E.F. Holby, P. Zelenay, W.-Q. Tao, Q. Kang, Lattice Boltzmann pore-scale investigation of coupled physical-electrochemical processes in C/Pt and non-precious metal cathode catalyst layers in proton exchange membrane fuel cells, Electrochimica Acta 158 (2015) 175–186.
[41] C. Huber, A. Parmigiani, B. Chopard, M. Manga, O. Bachmann, Lattice Boltzmann model for melting with natural convection, International Journal of Heat and Fluid Flow 29 (2008) 1469–1480.
[42] L. Chen, Q. Kang, B.A. Robinson, Y.-L. He, W.-Q. Tao, Pore-scale modeling of multiphase reactive transport with phase transitions and dissolution-precipitation processes in closed systems, Physical Review E 87 (2013) 043306.
[43] L. Chen, L. Zhang, Q. Kang, H.S. Viswanathan, J. Yao, W. Tao, Nanoscale simulation of shale transport properties using the lattice Boltzmann method: permeability and diffusivity, Scientific Reports 5 (2015) 8089.
[44] M. Wang, Q. Kang, N. Pan, Thermal conductivity enhancement of carbon fiber composites, Applied Thermal Engineering 29 (2009) 418–421.
[45] M.M. Tomadakis, S.V. Sotirchos, Ordinary and transition regime diffusion in random fiber structures, AIChE Journal 39 (1993) 397–412.
[46] P.A. García-Salaberri, J.T. Gostick, G. Hwang, A.Z. Weber, M. Vera, Effective diffusivity in partially-saturated carbon-fiber gas diffusion layers: Effect of local saturation and application to macroscopic continuum models, Journal of Power Sources 296 (2015) 440–453.
[47] R. Carta, S. Palmas, A.M. Polcaro, G. Tola, Behaviour of a carbon felt flow by electrodes Part I: Mass transfer characteristics, J Appl Electrochem 21 (1991) 793–798.
[48] Q. Kang, P.C. Lichtner, D. Zhang, An improved lattice Boltzmann model for multicomponent reactive transport in porous media at the pore scale, Water Resources Research 43 (2007).
[49] T. Zhang, B. Shi, Z. Guo, Z. Chai, J. Lu, General bounce-back scheme for concentration boundary condition in the lattice-Boltzmann method, Physical Review E 85 (2012) 016701.
[50] X. Shan, H. Chen, Lattice Boltzmann model for simulating flows with multiple phases and components, Phys. Rev. E 47 (1993) 1815–1819.
[51] H. Li, C. Pan, C.T. Miller, Pore-scale investigation of viscous coupling effects for two-phase flow in porous media, Physical Review E 72 (2005) 026705.
[52] A.G. Yiotis, J. Psihogios, M.E. Kainourgiakis, A. Papaioannou, A.K. Stubos, A lattice Boltzmann study of viscous coupling effects in immiscible two-phase flow in porous media, Colloids and Surfaces A: Physicochemical and Engineering Aspects 300 (2007) 35–49.
[53] M.L. Porter, E.T. Coon, Q. Kang, J.D. Moulton, J.W. Carey, Multicomponent interparticle-potential lattice Boltzmann model for fluids with large viscosity ratios, Physical Review E 86 (2012) 036701.